A 1.1-mW Ground Effect-Resilient Body-Coupled Communication Transceiver With Pseudo OFDM for Head and Body Area Network

Wala Saadeh, *Member, IEEE*, Muhammad Awais Bin Altaf, *Member, IEEE*, Haneen Alsuradi, *Student Member, IEEE*, and Jerald Yoo, *Senior Member, IEEE*

Abstract—This paper presents a body-coupled communication (BCC) transceiver (TRX) that mitigates all the practical impairments of the body channel at once. The proposed pseudo orthogonal frequency-division multiplexing (P-OFDM) TRX combines baseband BPSK–OFDM with frequency-shift keying (FSK) to alleviate the impacts of variable ground effect and variable skin-electrode contact impedance, which have been the two major issues on the BCC. It can tolerate up to 20 dB of channel gain variation with measured bit error rate improvement of >70% compared to FSK modulation alone. The RC relaxed contact impedance monitor continuously monitors and compensates the variable skin-electrode contact impedance at both transmitter (TX) and receiver (RX). The proposed power-gated 8-point inverse fast Fourier transform/fast Fourier transform with no floating-point multipliers (FPMs) reduces the gate count and power by 54% and 30% compared to conventional FPMs, respectively. Additionally, the simple floating-point adder (FPA) reduces the gate count and energy consumption by 34% and 20% compared to conventional FPAs, respectively. A high input impedance glitch-free FSK demodulation RX with variable threshold limiter and all digital cycle correction is also proposed to support a scalable data rate (200 Kbps–2 Mbps). The 0.54 mm^2 TRX in 65-nm CMOS consumes 1.1 mW.

Index Terms—Body area network (BAN), body-coupled communication (BCC), frequency-shift keying (FSK), orthogonal frequency-division multiplexing (OFDM), pseudo OFDM (P-OFDM).

I. Introduction

HEAD and body area network (HBAN) is an attractive mean to provide communication between low-power and small size devices that are on and around the human body [1], [2]. These devices range from monitoring
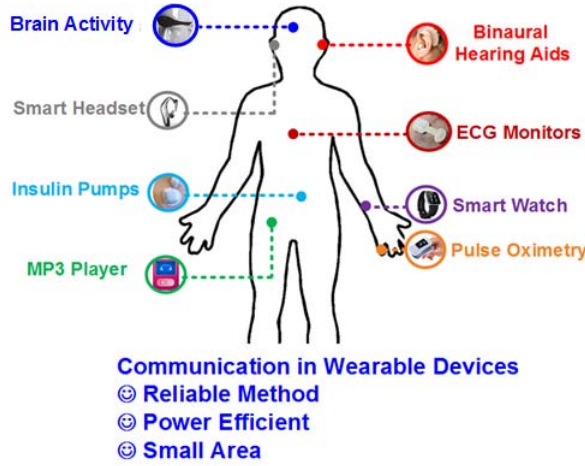
W. Saadeh and M. A. B. Altaf were with the Department of Electrical Engineering and Computer Science, Masdar Institute of Science and Technology, Abu Dhabi 54224, United Arab Emirates. They are now with the Electrical Engineering Department, Lahore University of Management Sciences, Lahore 54792, Pakistan.

H. Alsuradi is with the Department of Electrical Engineering and Computer Science, Masdar Institute of Science and Technology, Abu Dhabi 54224, United Arab Emirates.

J. Yoo was with the Department of Electrical Engineering and Computer Science, Masdar Institute of Science and Technology, Abu Dhabi 54224, United Arab Emirates. He is now with the Department of Electrical and Computer Engineering, National University of Singapore, Singapore 117585 (e-mail: jyoo@nus.edu.sg).

Color versions of one or more of the figures in this paper are available online at http://ieeexplore.ieee.org.

Digital Object Identifier 10.1109/JSSC.2017.2713522

patient vitals to on-device processing and from delivering the e-records of one's health and information to data storage and logger. Recent advances in smart devices may utilize HBAN to provide an augmented reality experience to a daily routine. Such devices can be used for rehabilitation of patients with disability, or for entertainment purposes [3], [4]. Fig. 1 shows the applications for HBAN that includes smart headsets, MP3 players, helmet-mounted displays, smart watches, smart shoes, and binaural hearing aids [5], along with the corresponding minimum data rate requirement of each application [6].

Conventional high-frequency communication transceiver (TRX) including Bluetooth, ZigBee, and ultra wide band (UWB) are not suitable for HBAN due to body shadowing effect and huge (~80 dB) attenuation when the antenna is in the vicinity of or attached to the human body [5], [8]. To overcome such obstacles, body-coupled communication (BCC) can be utilized for an energy efficient implementation with sufficient data rate and communication distance capabilities [9], [10], where the human body serves as a communication channel. Fig. 2 shows the trend of, date rate, power consumption, and energy/bit of the state-of-the-art TRXs presented in the literature for HBAN. BCC lies in a region of relatively high data rate with minimum energy/bit consumption compared to zigbee, bluetooth, and UWB. Despite the advantages of the BCC channel, there are certain challenges that must be tackled to make it a practical BAN solution: 1) weak and varying ground path (return signal path) connection denoted as variable ground effect, 2) interference, 3) signal multipath problem [11], and 4) variable skin-electrode contact impedance [12]. These challenges will be explained in detail in Section II.

Previous state-of-the-art work for building BCC TRXs only attempt to mitigate the interference [5] and/or variable skin-electrode contact impedance [12]. However, the proposed solutions are not optimal in terms of power and area usage. Reference [13] provides a standard compatible BCC TRX while [14], [15] provide high data rate transmission, but tackle neither the ground effect, signal multipath nor the varying skin-electrode impedance problems. Reference [16] presents a solution for the signal multipath issue but with a large area. Reference [17] presents an orthogonal frequency-division multiplexing-(OFDM) based transmitter (TX) only with complex implementation to overcome the peak-to-average-power ratio. This paper presents a BPSK pseudo OFDM (P-OFDM) TRX which for the

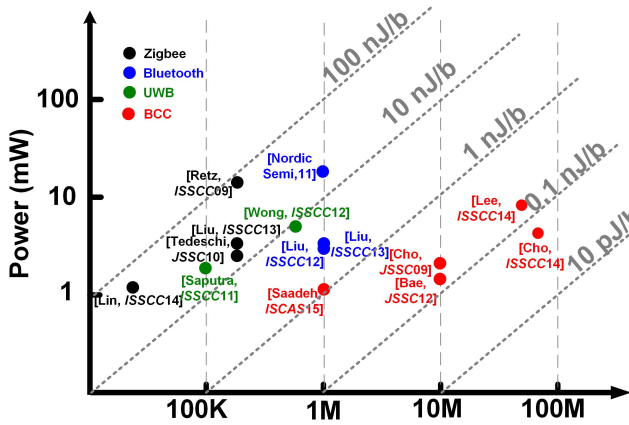| Application	Data Rate
Binaural Hearing Aids	1Mbps
ECG Monitors (12 leads)	288Kbps
EMG Monitor	320Kbps
Brain Activity	300Kbps
ZEN MP3 Players	2Mbps
Music for Headset	1.4Mbps
Fitness Monitor	500Kbps
Artificial Retina	50-700Kbps
Pulse Oximetry	1Kbps

Fig. 1.   HBAN applications [6].

Fig. 2.   Recent TRXs trend in terms of energy per bit, power consumption versus data rate.

Fig. 3.   BCC coupling methods. (a) Magnetic. (b) Galvanic. (c) Capacitive.

first time in literature, mitigates the effects of variable ground effect, signal multipath, interference, and varying skin-electrode impedance problems of BCC, all at once with minimum area and power consumption [18]. It also introduces a glitch-free frequency-shift keying (FSK) demodulation (DEM) receiver (RX) to support a scalable data rate (200 Kbps–2 Mbps) that can be utilized for a wide range of applications in HBAN.

The paper is organized as follows. Section II describes the behavior of capacitive coupling BCC with channel path loss measurements and it explains the variable skin-electrode contact impedance. Section III explains the proposed P-OFDM TRX implementation that includes 8-point inverse fast Fourier transform/fast Fourier transform architecture; glitch-free FSK DEM RX; and *RC* relaxed contact impedance monitor circuit. Measurement and verification results are described in Section IV. Finally, Section V concludes the paper.

II. CAPACITIVE COUPLING BODY CHANNEL COMMUNICATION

Three conceptually different methods exist to transmit a signal through the body: magnetic resonance coupling, galvanic coupling, and capacitive coupling [19], [20]. In mag-
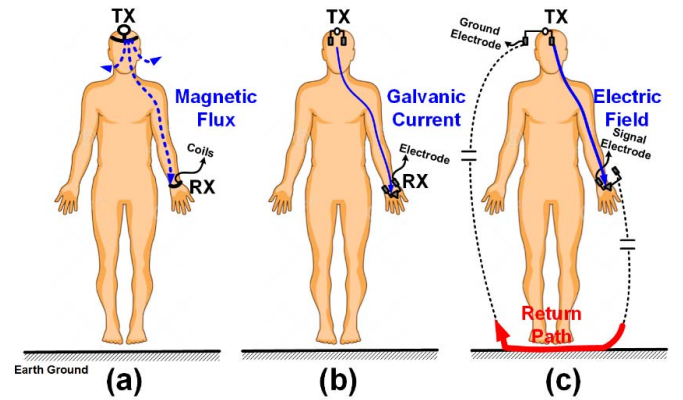
netic resonance coupling [Fig. 3(a)], resonant coils are used to generate and receive magnetic energy [19], where it is difficult to maintain constant coil resonance due to motion artifacts. In addition, the use of coil limits on-chip integration. For both BCC electric transmission methods (galvanic and capacitive couplings), the BCC TRX nodes consist of TX, RX, and electrodes which replace antenna used in typical RF communications. In galvanic coupling [Fig. 3(b)], two electrodes are in direct contact with the skin at the TX and pass a differential signal to the body. The signals are captured by another pair of electrodes at the RX. This method is relatively independent of the environmental changes because it does not involve the external earth ground as a return path. However, due to its high path loss over the 1-MHz range, it is rather preferred for short distances (<15 cm) between the TX and the RX with limited data rate [21], [22]; hence it limits the target applications significantly.

On the other hand, in capacitive coupling [Fig. 3(c)], the single-ended signal electrodes of both TX and RX are attached to the skin while the ground electrodes are left floating. There is no need for direct human skin contact with the signal electrodes, and the close proximity of the electrodes to the body is sufficient [20]. The TX generates an electric potential through its signal electrode, inducing an electric field in the body that is sensed by the RX's signal electrode. The floating ground electrodes are coupled to earth ground
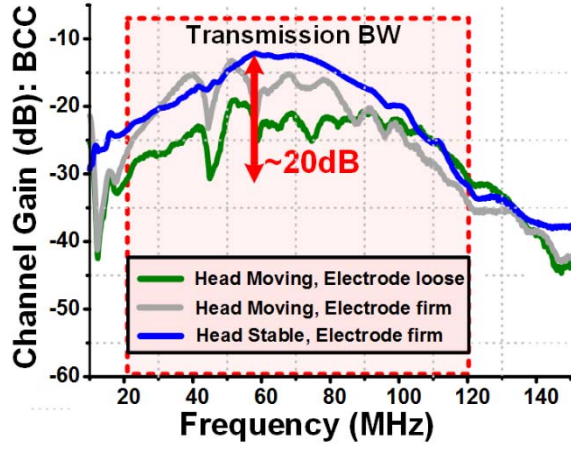
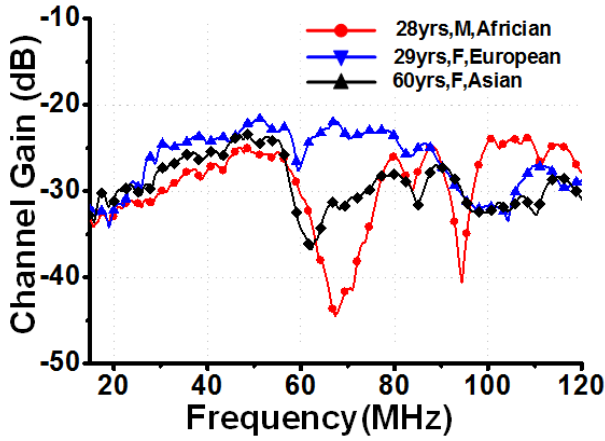Fig. 4.   Measured path loss for different body postures.

Fig. 5.   Measured path loss for different subjects (channel length: 100 cm).

through the air, creating a weak, varying return path [23]. The existence of an external path through parasitic capacitance means that capacitive coupling is suitable for wearable devices (i.e., attached to the surface of the human body), and when compared to galvanic coupling, it offers less path loss and a relatively higher frequency range of operation, between 20 and 120 MHz, which enables higher data transmission rates compared to galvanic coupling [23]. In addition, it does not requires the use of extra coils at both TX and RX as compared to magnetic resonance coupling [19]. In this paper, capacitive coupling BCC is utilized due to its superior performance compared to the other coupling mechanisms and in order to achieve higher data rate and larger communication distances that support different HBAN application requirements. However, there are critical challenges that need to be tackled for precise operation of the TRX utilizing capacitive coupling BCC for HBAN applications.

A. Challenges in Capacitive BCC

The major challenges encountered by capacitive BCC, which so far limited the BCC to be adopted widely in wearable applications, are as follows:
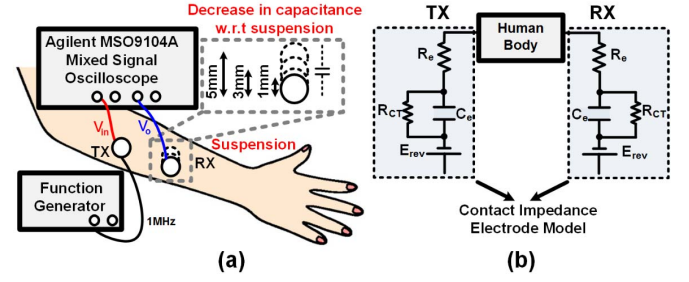

Fig. 6.   (a) Measurement setup for contact impedance measurement with respect to the electrode suspension from the skin surface. (b) Simplified skin-electrode contact impedance model.
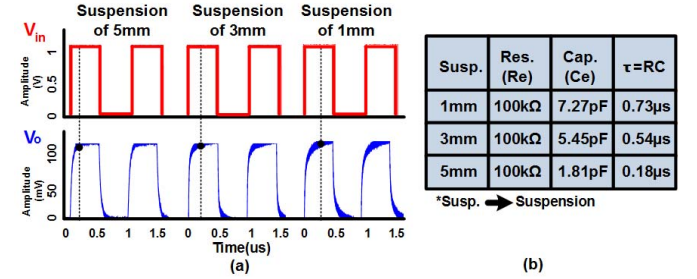

Fig. 7.   (a) *RC* settling time analysis for various suspensions. (b) Measurement summary with various electrode suspension from the skin.
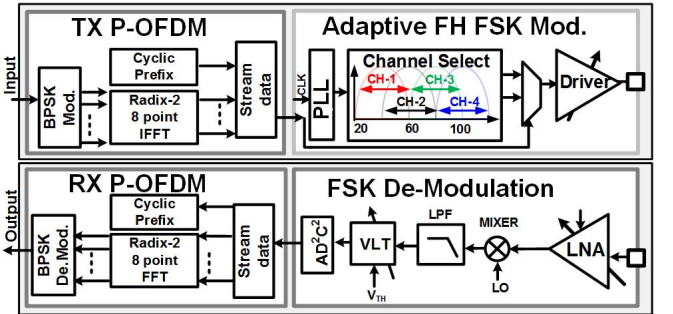

Fig. 8.   Block diagram of the proposed PSK P-OFDM TRX.

1) Variable Ground Effect: The capacitive BCC channel is formed via capacitive coupling between the human body and the external earth ground. Since the human subject using this channel is not fixed during the communication time and can attain different postures and perform unpredictable movements, thus, the quality of communication is highly influenced by subject's movements. Moreover, any variations in the TRX height from the earth ground can affect the channel gain significantly [24]. These conditions can be denoted as variable ground effects [25], [26].

2) Interference: The BCC channel can be affected by potential static or dynamic nearby transmissions occurring in the same frequency band. This vulnerability to other channel impairments may corrupt the signal.

3) Multipath: The signal transferring from TX to RX can follow multiple paths, which lead to multiple copies of the same signal to be detected at the RX and added to each other in a constructive or destructive way [5], [11].
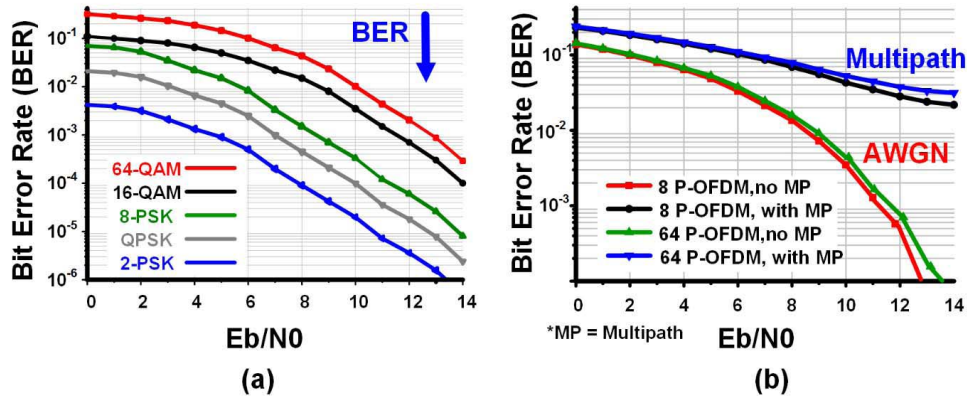
Fig. 9. BER comparison between (a) different constellations types in P-OFDM and (b) 8 and 64 subcarriers in P-OFDM.

4) Variable Skin-Electrode Impedance: The skin-electrode connection is not continuously fixed during the transmission time which will affect the channel quality due to variation in the contact impedance between the skin and electrodes [12].

B. Variable Ground Effect Channel Path Loss Measurements

The human body involves the skin, muscles, fats, and bones which imply different conductivity of the human body and multiple signal paths depending on the on-body location of both TX and RX and the length of the transmission channel [11], [24]. Therefore, longer transmission distance results in multiple higher impedance forward paths and also susceptible to more parasitic capacitances as compared to shorter one which reduces the channel gain [5]. In general, the channel gain flows a band-pass filter shape with a band pass a range of 20–120 MHz [25]. However, the channel gain is different at each frequency, which indicates the human channel exhibits frequency selective behavior due to the multipath effect caused by multiple forward paths and the variable ground effect [24]. This effect can be seen clearly at longer channels. Fig. 4 shows the measured path loss for different posters of the human body in the transmission bandwidth (20–120 MHz). Movement and loose electrode connection may lead up to 20 dB of gain variations. This is due to the variable parasitic capacitances between the ground electrodes and the earth ground, and the variable skin-electrode impedance [24], [25].

Different subjects have different ratios of body components such as fat and muscle that causes different conductivity in the multiple forward paths of the body channel. In addition, they have different heights that also affects the parasitic capacitances in the return path. Fig. 5 shows the channel gain for three different healthy human subjects (two females and one male, with age: 28–60 years, body mass index: 23.8–30.1, different ethnicity) for the same posture of 100 cm (left arm to right arm) communication. It can be observed that there is also a significant difference (up to around 20 dB) in channel gain from person-to-person too. These channel gain variations require a TRX design that mitigates the effect of gain variations on the communication quality.
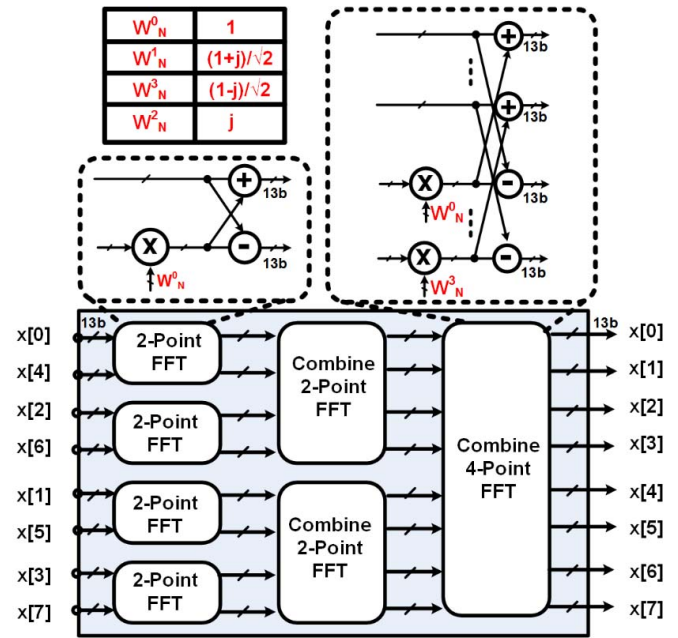

Fig. 10. Radix-2 8-point FFT implementation.

C. Skin-Electrode Impedance Variation

The skin-electrode contact impedance is an important factor to consider in BCC, since large and varying contact impedance can degrade the communication quality. In general, dry electrodes have higher contact impedance compared to wet electrodes [27]. Since the outer layer of skin is a dry dielectric, we use wet electrodes (Ag/AgCl) to establish a strong conductive path from the skin to TX and RX. However, by using the wet electrodes for a long time, the electrolyte dries out and the contact impedance changes [27]. Moreover, the presence of air gaps between the electrodes and skin, especially if there is hair on the skin surface or slight detachment of electrodes, varies the series impedance of the input path. Therefore, both TX and RX should consider this skin-electrode impedance variation, and continuously monitor the skin-electrode impedance to compensate for any losses in channel gain [28].

Measurement and analysis are also performed to compute the variation in skin-electrode contact impedance for

different skin-electrode suspensions from the surface of the skin (i.e., skin-electrode non-contact distance); this reflects the practical situation where the electrode is not firmly attached to the skin. Fig. 6 shows the measurement setup to estimate the impedance at different suspensions along with simplified skin-electrode contact impedance model that is adopted for modeling the real system [27]. In this model, C_e represents the double layer capacitance, R_{CT} is the charge transfer resistance, R_e is the sum of the lead and electrolyte resistances, and E_{rev} represents the reversible or equilibrium potential [27]. In this measurement, a pulse source (V_{in}) of 1 MHz is transmitted through the human arm and then measured at the RX side (V_o). Initially, both TX and RX electrodes are firmly connected to the human skin, and then the RX electrodes are tested for different suspension distances between electrode and skin. The 1-MHz frequency is selected by performing different trails to ensure settling of the output with sufficient margins for different suspensions values. The contact impedance is primarily controlled by the capacitive component (C_e) of the skin-electrode interface due to suspension [12], [29]. By increasing the suspension between skin and electrode, the C_e value will decrease. Therefore, any changes in the capacitance value will be reflected as variation in the time constant of received/transmitted signal. Fig. 7(a) shows the measurement results at different suspension distances at RX side while the TX electrode is firmly attached to the body, as shown in Fig. 6. The table in Fig. 7(b) summarizes the measured RC values under different suspensions and impedance values. The aim of these measurements is to evaluate only the variation of capacitance between skin and electrode at RX side for different suspension distance. Therefore, in the calculation/evaluation, the effect of channel capacitance and TX contact impedance is neglected.

This analysis shows the relative change in capacitance value with respect to the suspension distance. To simplify the computation, α is assumed to be channel gain. RC variation at different suspension distances are measured along with corresponding settling time (t_s), where t_s is the time value when signal reach its ~99% of maximum value ($t_s = 5\tau$). By using the t_s, the relative change in capacitance for different suspension distances can be obtained as

$$V_o = \alpha V_{in}(1 - e^{-t/\tau}) \tag{1}$$

where $\tau = R_e C_e$

$$V_o \approx \alpha V_{in} \text{ when } t = t_s = 5\tau$$

where V_o is the output signal observed at the RX, V_{in} is the input signal applied at the TX, t is the time in seconds, τ is the time constant, and α is the channel gain. Suspensions of 1, 3, and 5 mm correspond to the capacitance value of 7.27, 5.45, and 1.81 pF, respectively.

III. PROPOSED TRANSCEIVER WITH PSEUDO-OFDM

The proposed scalable data rate (200 Kbps–2 Mbps) TRX adopts P-OFDM [5] to achieve reliable transmission that mitigates variable ground effect, variable skin-electrode contact impedance, signal multipath, and interference issues, all
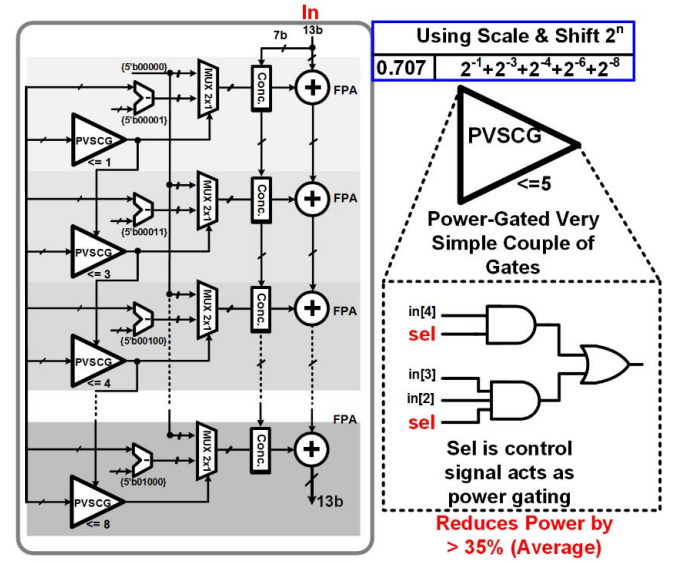

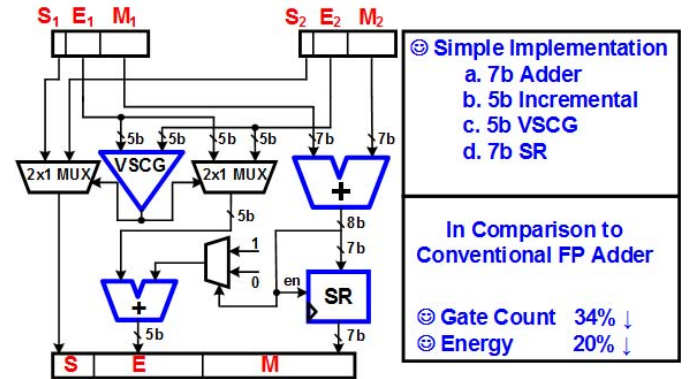Fig. 11. Proposed power-gated DSR2 implementation.

Fig. 12. Implementation of the simple FPA.
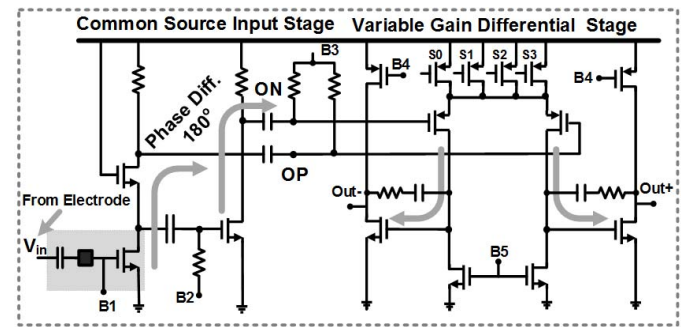
Fig. 13. Proposed high input impedance reconfigurable gain LNA.

at once. In the P-OFDM, the actual physical signal transmitted on the channel is based on the FSK, and therefore the method does not exploit the orthogonal aspect of subcarriers, but rather utilize the higher available bandwidth in body channel (when compared to RF on body), to effectively mitigate the ground effect, and signal multipath and thus improve the bit error rate (BER) performance [5]. The conventional approach to mitigate all the mentioned channel impairment is by adopting

Fig. 14.   (a) Block diagram of proposed FSK DEM RX. (b) Frequency domain representation of DEM process (1) at the input of mixer, (2) at the output of mixer, and (3) at output of LPF.
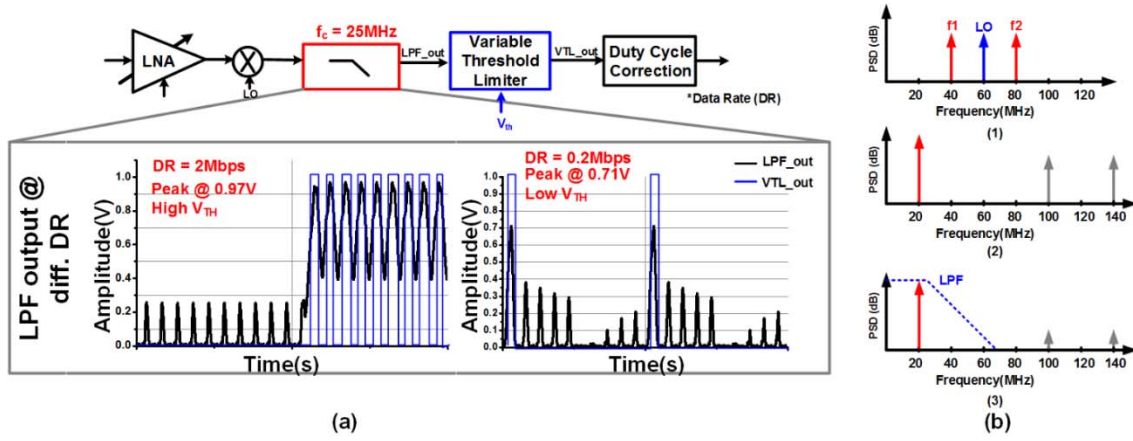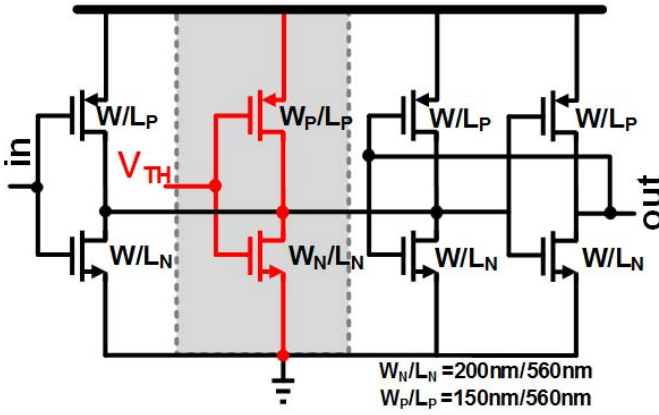

Fig. 15.   Schematic of the proposed VTL.

Fig. 16.   (a) Block diagram of AD^2C^2 and (b) its timing diagram.
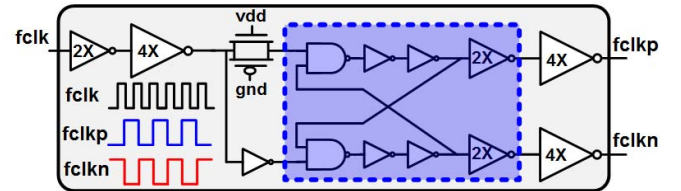
Fig. 17.   Schematic of out-of-phase clock signals generator.

OFDM [17] or P-OFDM [5] but requires significant large area and processing power for the IFFT/FFT implementation, which limits the on-chip application. Therefore, we are proposing an 8-point IFFT/FFT to overcome the issue. The overall block diagram of the proposed TRX is shown in Fig. 8. The FSK modulation is combined with 4 channel adaptive frequency hopping that operates in the 20–120 MHz band for interference-resilient transmission [30]; this band is selected for minimal path loss [5]. In the proposed system, the PLL at TX side is designed to provide the clock for the RX.

A. Radix-2 8-Point FFT Implementation

In the baseband OFDM TX and RX, a PSK constellation with 8-point IFFT/FFT is utilized to perform symbol generation and recovery functionality as opposed to 16-QAM and 64-point IFFT/ FFT in [5]. Fig. 9(a) shows BER comparison between the different constellation types that can be utilized in P-OFDM. The BPSK demonstrates the minimum BER as compared to other constellation methods, which make it tolerable to the variable channel gain. Fig. 9(b) shows the BER comparison between the 16-QAM P-OFDM for a different number of subcarriers utilized in IFFT/FFT block. It can be noticed that the number of subcarriers utilized in the
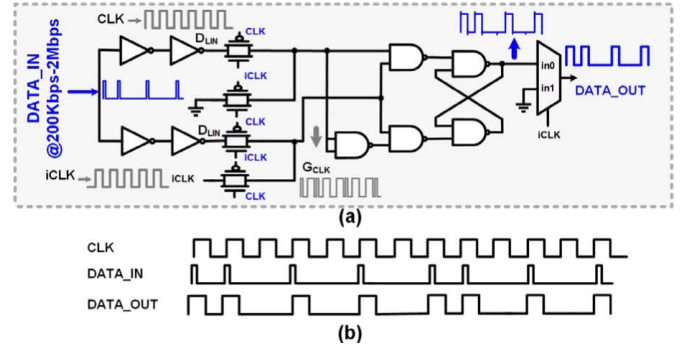
IFFT/FFT block does not affect the BER performance of the P-OFDM modulations. The number of subcarriers utilized in the FFT/IFFT block and the sampling clock decide the data rate of the P-OFDM modulations. Utilizing a lower number of subcarriers allows a simpler design of FFT/IFFT block at the cost of increasing the sampling clock speed to achieve the same data rate. Achieving date rate ≥ 10 Mbps is not feasible with a small number of subcarriers in P-OFDM due to a significant increase in the sampling clock speed. The 8-point P-OFDM has data rate limit of up to 10 Mbps due to a significant increase in the sampling clock speed but since the BCC applications mentioned in Fig. 1 only requires up to 2 Mbps, this is not a big issue. Table I shows the comparison between this work (8-point BPSK P-OFDM) [18] and the 64-point 16-QAM P-OFDM [5] in terms of gate count, area, power, BER, and the supported data rate. Power and area reductions of 93% and 85%, respectively, are reported

Fig. 18.   RRCIM implementation block diagram.

TABLE I
COMPARISON BETWEEN 8-POINT PSK P-OFDM AND
64-POINT 16-QAM P-OFDM [5]

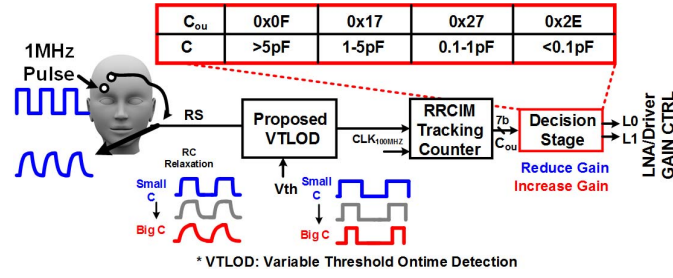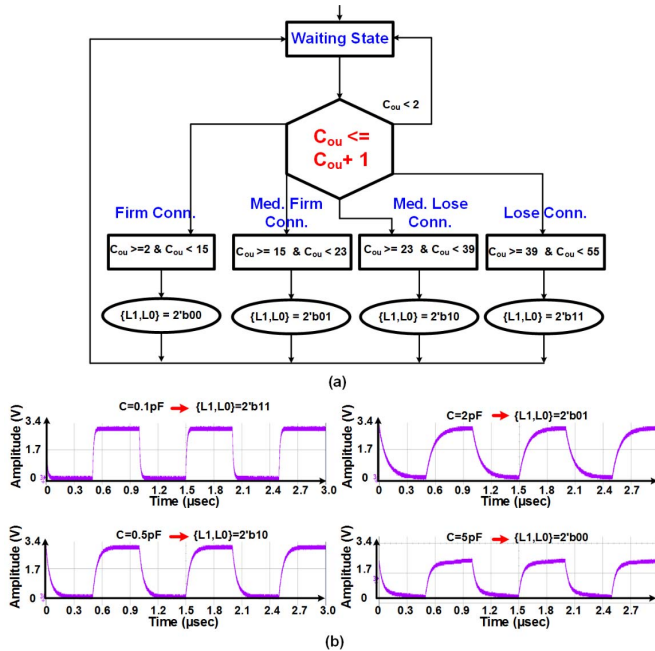|	64 P-OFDM 16 QAM [5]	8 P-OFDM, BPSK This Work
Gate Count	113K	34K
Active Area	1.8mm^2	0.25mm^2
Power Consumption	300uW	20uW
BER @ Eb/N0 = 10	2.0x10^{-3}	4.0x10^{-5}
High (≥10Mbps) Data Rate Support	O	X

Fig. 19.   RRCIM. (a) State flow diagram for the decision block. (b) Different measurements of the RS for different skin-electrode contact capacitance values.

by utilizing 8-point P-OFDM as opposed to the 64-point P-OFDM [5].

The main block in the proposed baseband OFDM TX and RX is the area and energy efficient 8-point IFFT/FFT with division by-square root of 2 (DSR2) block. The proposed 8-point FFT implementation is based on a Radix-2 algorithm, as shown in Fig. 10, the constants to be multiplied at each stage are known *a priori*. The constants in the first two stages are either (1) or (j) and are realized by floating-point addition/subtraction operations; therefore, no dedicated floating-point multipliers (FPMs) are utilized. However, in the third stage, the multiplications of the constants are addition/subtraction operation followed by division by the square root of 2. The last stage's multiplication operation is implemented using the proposed power-gated DSR2, which is realized by using only add and subtract operations, as shown in Fig. 11. The proposed DSR2 reduces the gate count by 54% compared to conventional FPM at a minimal cost of precision loss (<2% of overall BER). Moreover, to further reduce the power consumption; the proposed implementation utilizes power-gated very simple couple of gates (PVSCG) and proposed floating-point adder (FPA). The PVSCG switches off the power supply of specific comparator when it is in the non-operational mode to reduce the leakage power consumption. During the DSR2 processing, the number of comparator utilization depends on the incoming input data value and on average the proposed PVSCG reduces the power consumption by 35% compared to the VSCG [5]. Gate count reduction of 34% and an energy reduction of 20% are achieved due to the proposed FPA implementation as shown in Fig. 12 compared to the conventional FPA.

B. FSK Demodulator

In the capacitive BCC, the RX input is coupled with surface electrodes that make it susceptible to high and varying electrode impedance. Therefore, the LNA input impedance is designed using a common source input stage to consider the high skin-electrode contact impedance (which is much higher than typical 50 Ω in RF) as shown in Fig. 13. The reconfigurable gain LNA provides a band-pass filter (20–120 MHz) behavior to reject out-of-band noise and eliminates the need for an additional external filter. The LNA supports wide gain settings (20–35 dB) to compensate for the variable channel path loss and the variable skin-electrode contact impedance. Moreover, dc coupling is utilized by incorporating an off-chip capacitor (0.1 μF) to reject the electrode dc offset that may corrupt the input signal significantly.

Conventional FSK DEMs with low-frequency direct conversion RX such as delay-locked loops (DLL) based or
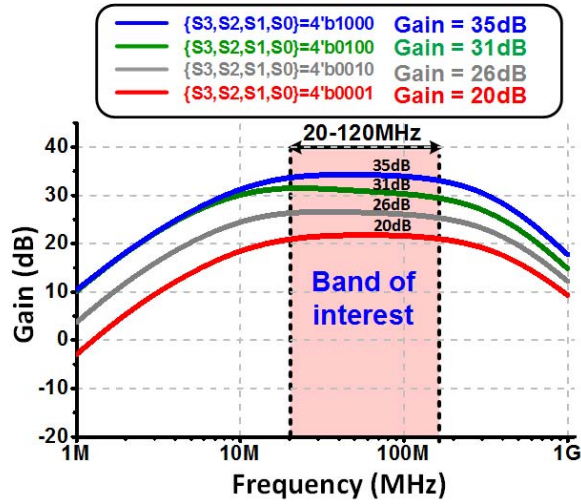
Fig. 20. Measured LNA gain and bandwidth.

Fig. 21. Measured output of VTL for variable threshold voltage.

fixed-time-delay DEM [12], [30] consume high power and large area. The proposed FSK DEM avoids using DLL to reduce area and power consumption by 90% and 65%, respectively, as compared to [12]. It is also capable of demodulating a scalable data rate signal (200 Kbps–2 Mbps) as compared to the miniaturized FSK DEM proposed in [5] that supports a single data rate only. The proposed DEM utilizes power and area efficient: 1) variable threshold limiter (VTL) and 2) all digital duty cycle correction (AD^2C^2) blocks to achieve data recovery at RX side, as shown in Fig. 14(a). The output of the low pass filter (LPF) is transformed to a full-swing square wave using the proposed variable threshold Schmitt–Trigger circuit that acts as a controlled limiter. The VTL allows the DEM to support scalable data rate since the LPF's output signal levels are changed by changing the data rate which requires a VTL to detect them precisely as shown for the cases of input data rate of 2 Mbps and 200 kbps in Fig. 14(a). The frequency domain representation of the DEM process of the incoming FSK modulated signal is shown in Fig. 14(b). As an example, the scenario of transmission via channel 2 is shown in Fig. 14(b)-(1), where the binary FSK frequencies are at 40 and 80 MHz and the mixer input clock [local oscillator (LO)] frequency of 60 MHz. The output of the mixer is shown in Fig. 14(b)-(2), with the frequencies generated by the mixing operation which will be applied to a LPF with a cutoff frequency of 25 MHz. The LPF output is shown in Fig. 14(b)-(3).

Fig. 15 shows the schematic of the proposed VTL, where the control voltage is added with an additional stage to decide the V_{HL}/V_{LH} of the limiter. V_{HL} is the input voltage at which output switches from high to low, and V_{LH} is the input voltage at which output switches from low to high. For high input threshold, the output pulse will be wider due to low V_{LH} and high V_{HL} and vice versa for low input threshold.

The output pulses generated from the VTL have a small duty cycle (1%–25% depending on the data rate). It is essential for the P-OFDM RX output to have 50% duty cycle such that they can match the exact original sent data format and can be easily detected at the input of P-OFDM symbol recovery block.
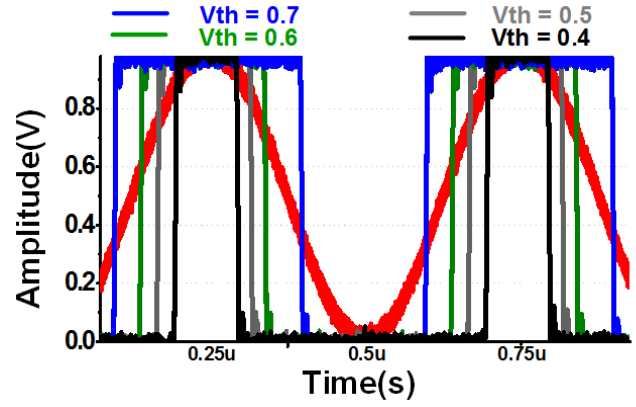
Received bit "1" with a duty cycle less than 50% may be not detected correctly at the P-OFDM symbol recovery block due to its short duration. Therefore, the AD^2C^2 circuit recovers the 50% duty cycle (DuC) of received (bit 1) for the DATA_IN signal as shown in Fig. 16(a). The delayed input data (D_{LIN}) and an internally generated clock (G_{CLK}) act as data and clock, respectively, to the cross-coupled NAND gate circuit [D-Flip-Flop (DFF)]. The D_{LIN} ensures input data to be processed by the DFF circuit and G_{CLK} enables double triggering of the DFF in the case of bit 1 is received which guarantees the positive and negative edges of D_{LIN} to have 50% DuC. This may cause glitches at the output [31], but we achieve glitch-free function by the MUX sampling the input at iCLK. In the case of no input data (bit 0), single triggering of DFF occurs to remove any parasitic charges. Fig. 16(b) shows the working of proposed AD^2C^2 with the help of timing diagram for a DATA_IN, DATA_OUT, and CLK. The AD^2C^2 consumes 0.62 μW at 2 Mbps which is 99% less than (80 μW) consumed by charge pump-based DuC detection and correction circuit [12].

A double balanced mixer is adopted which is based on Gilbert cell. All inputs and output signals are differential with an out-of-phase carrier clock signals. Fig. 17 shows the proposed out-of-phase clock signal generator to ensure correct operating of the mixer. The implemented out-of-phase clock generator is based on cross-coupled NAND gate to guarantee a mutual exclusion; a NAND gate's output goes logic low when both its inputs are high. In the out-of-phase clock generation, NAND-based implementation is preferred over the NOR [3] to reduce the propagation delay, and to ensure 50% duty cycle out-of-phase clock generation even at the LO frequency of 100 MHz. To prevent the probability of two cross-connected NAND gates circuit to have either low or high output at the same time for any input combination, a delay between one NAND gate's output changing and the other NAND gate seeing the new value as input is inserted. Moreover, sufficient time margin in the form of delay unit is also provided on the input side to safeguard the signal against any glitches. The out-of-phase clock generator guarantees the effect of LO feed through to the output to be eliminated.

C. RC Relaxed Contact Impedance Monitor

Skin-electrode contact impedance varies during the BCC transmission which results in a channel gain variation of
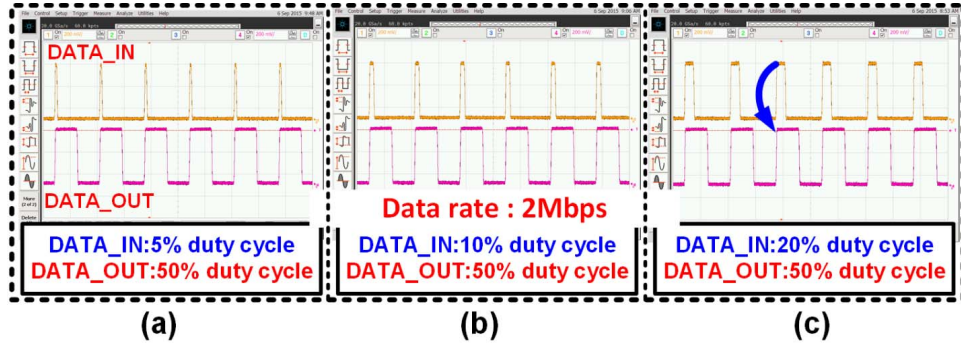
Fig. 22.   Measured AD^{2}C^2 output for input duty cycle of (a) 5%, (b) 10%, and (c) 20%.
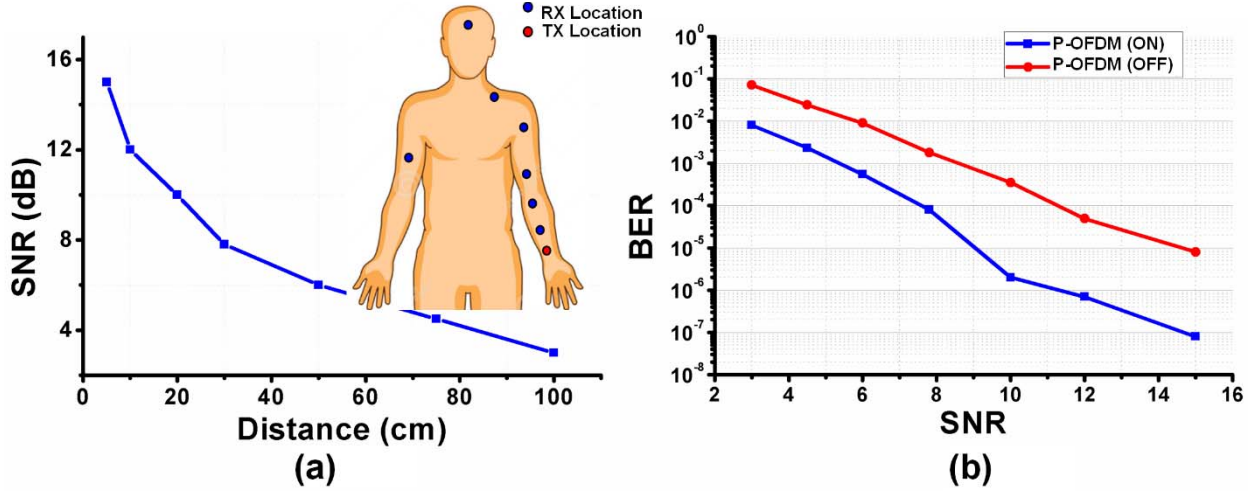

Fig. 23.   (a) Measured SNR with communication distance and locations of TX and RX. (b) Measured BER performance of the P-OFDM when it is ON and OFF.

more than 10 dB [12]. These variations can occur at both TX and RX sides which require continuous monitoring and gain compensation mechanisms. Therefore, an *RC* relaxed contact impedance monitor (RRCIM) is proposed to adapt the gain of driver/LNA at both TX and RX, respectively. The key idea is to utilize the *RC* relaxation variance of a 1-MHz clock signal (available on chip) to update the gain of driver/LNA; no additional current injection is required for skin-to-electrode impedance monitoring as opposed to [32], which makes it a power-efficient solution. RRCIM is responsible for automatic control of the gain settings of LNA and driver based on the measured skin-electrode contact impedance during each cycle of the 1-MHz signal.

Fig. 18 denotes the block diagram of the RRCIM in which a pulse signal (1 MHz) is transmitted via skin (*RC* network) at one node and detected from the adjacent node [29]. In the band-of-interest, the contact impedance is dominated by the capacitive component of the skin-electrode interface, with a finite *RC* time constant [12]. Therefore, any changes in the capacitance value will be reflected as variation in the time constant of received signal (RS). Fig. 19(a) shows the state flow diagram of the decision stage for the RRCIM block, whereas Fig. 19(b) shows the measured RS for different skin-electrode contact capacitance values. This RS will be fed to a VTL block that generates noticeably different width pulses for

different capacitance values. The variable pulse width enables the on-chip counter (working at CLK = 100 MHz) to decode the corresponding pulse width duration. Moreover, a lookup table-based decision circuit maps the counted value to one of 4-preset control settings for LNA/driver gain accordingly to compensate for the losses. L1 and L0 are the control switches for a 2-to-4 decoder that will set the values of the S0–S3 switches in order to control the gain of the driver/LNA in the TX and RX, respectively. Unlike conventional current injection type [12], the RRCIM does not need pure sine wave current generation. As a result, it consumes 4 μW, which is >78% less power compared to [12], [33].

IV. MEASUREMENT RESULTS

The gain settings in the proposed implementation are configured automatically based on the skin-electrode impedance variation adopted by the RRCIM circuit. Fig. 20 shows the measured different gain settings of the LNA controlled by S0–S3 in the intended band (20–120 MHz) with gain values of 20, 26, 31, and 35 dB. When the skin-electrode connection is loose, the input RX signal is small and require higher gain, whereas lower gain is required for a firm skin-electrode connection. The noise ?gure and the sensitivity will vary for the different gain settings [5]. Low noise figure, higher sensitivity, and high gain are desired for weaker input signal
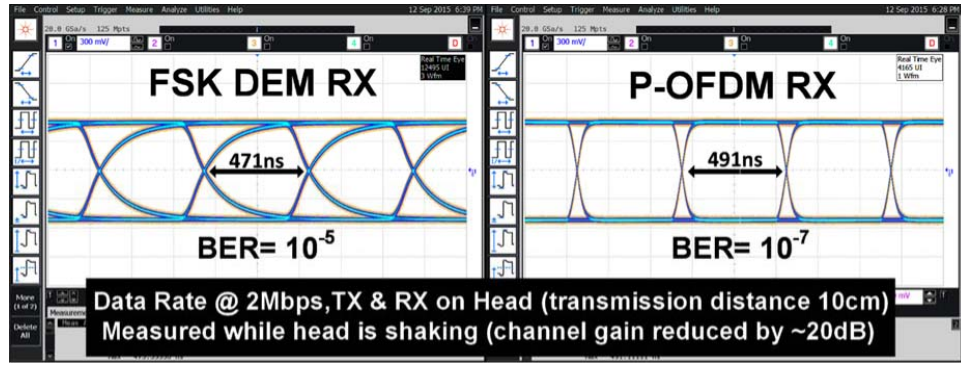
Fig. 24. Measured eye diagram and BER of P-OFDM versus FSK.

strength. The noise figure of LNA can be adjusted by changing the gain, from 3.2 to 8.9 dB, corresponding to the sensitivity of -88.5 to -83.1 dBm. Relatively low power is consumed to achieve a higher noise figure in comparison to the low noise figure of LNA, for instance; the gain value of 20 dB in the implemented system does not require a small noise figure (3.2 dB), therefore power consumption can be reduced by high noise figure (8.9 dB) to achieve the same performance.

The measured output of the VTL for the different threshold is shown in Fig. 21. The width of the output pulse depends on the input threshold voltage (V_{th}), where the smaller the V_{th}, the smaller the pulse width, and the larger the V_{th} value, the bigger the pulse width. Fig. 22 shows the measured AD^2C^2 output for an input signal with a DuC of 5%, 10%, and 20%, where the output meets the 50% DuC signal.

Fig. 23 shows how the SNR and BER are affected by increasing the communication distance (5–100 cm). For a communication distance below 50 cm, it is tested on a single arm. However, the higher communication distances >50 cm are tested as follows:

1) TX on arm (near the wrist) and RX on the shoulder (50 cm).
2) TX on arm (near the wrist) and RX on the head (75 cm).
3) TX on arm (near the wrist) and RX on the other arm (100 cm).

Fig. 23(a) shows the measured SNR at different communication distances where the SNR drops at high communication distances. The BER is also measured for the cases (P-OFDM ON/OFF) for the same communication distances as shown in Fig. 23(b). It can be noticed a BER improvement of $>70\%$ when the P-OFDM is used. For higher communication distances >100 cm, the SNR value drops below 2 dB and BER rises to $>10^{-2}$.

Fig. 24 shows the eye diagram and BER measurements at the outputs of both P-OFDM RX and the FSK DEM RX with body channel of 10 cm, where the proposed P-OFDM improves the BER by two-order of magnitude compared to FSK.

The proposed P-OFDM TRX is implemented in 65-nm-1P7M CMOS process with the core area of 0.54 mm^2, while consuming 1.1 mW at 1.1-V supply, which is 50% and 80% less power as compared to [12] and [13], respectively,
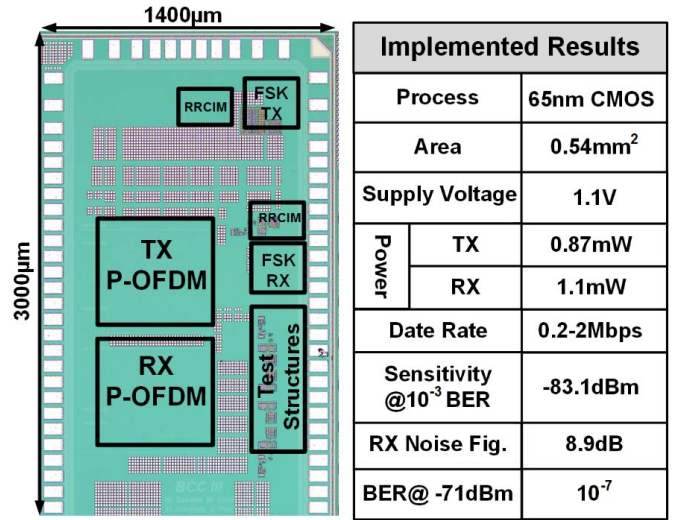

Fig. 25. Die Photograph of the P-OFDM and performance summary.

Implemented Results	
Process	65nm CMOS
Area	0.54mm^2
Supply Voltage	1.1V
Power — TX	0.87mW
Power — RX	1.1mW
Date Rate	0.2-2Mbps
Sensitivity @10^{-3} BER	-83.1dBm
RX Noise Fig.	8.9dB
BER@ -71dBm	10^{-7}

as shown in Fig. 25. It alleviates the effects of environmental variables on the BCC channel quality. In addition, it also mitigates the signal multipath and interference problems while supporting a scalable data rate (200 Kbps–2 Mbps). The measured RX sensitivity at a data rate of 2 Mbps is -83.1 dBm with a noise figure of 8.9- and 1-dB compression point of -18.9 dBm.

Fig. 26(a) and (b) shows the distribution of the power and area, respectively, of the proposed P-OFDM TRX. The P-OFDM TX and RX digital blocks are consuming 20 μw each. The power breakdown of the RX is shown in Fig. 26(c), where the maximum power (0.69 mW) is consumed by the PLL since its providing the clock for the RX in the current implementation. The proposed FSK DEM significantly reduces the RX power. It should be noted that by adopting 8-point IFFT/FFT with DSR2 and PVSCG reduces the area of the P-OFDM symbol generation and recovery blocks significantly; compared with [5], we achieved 74.6% reduction in area. Table II summarizes the performance comparison of proposed P-OFDM TX with the state-of-the-art works and shows the implemented design as first in the literature to mitigate ground path, contact impedance variation, and multipath interference issues.
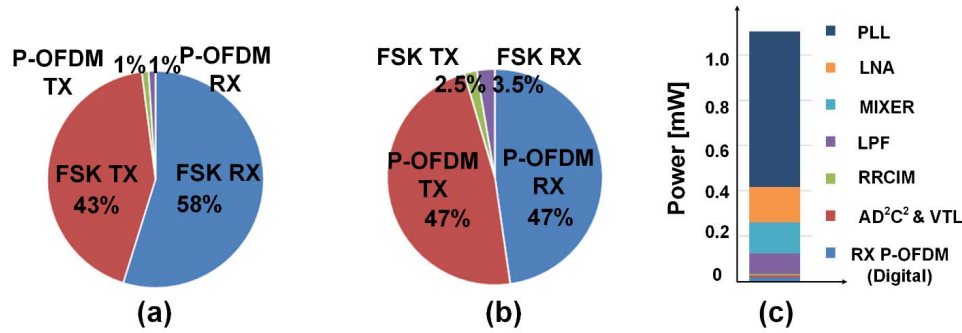
Fig. 26.   (a) Power and (b) area of the distribution of the P-OFDM TRX. (c) RX power breakdown.

TABLE II
COMPARISON WITH THE STATE-OF-THE-ART WORK TRXS

Parameter	J. Bae, *JSSC* 2012 [12]	J. Lee, *ISSCC* 2014 [15]	H. Cho, *ISSCC* 2015 [14]	H. Cho, *JSSC* 2015 [13]	W. Saadeh, *JSSC* 2017 [5]	This Work
Technology	180nm CMOS	65nm CMOS	65nm CMOS	0.13um SMIC	65nm CMOS	65nm CMOS
Frequency Band	40-120MHz	40-120MHz	20-60MHz 140-180MHz	18.375-23.625MHz	20-120MHz	20-120MHz
PHY/ Modulation	Double FSK	3-Level Walsh	BPSK-OOK	BPSK	64 P-OFDM 16 QAM	8 P-OFDM BPSK
Multipath Mitigation	X	X	X	X	O	O
Ground Effect Mitigation	X	X	X	X	X	O
Skin-Electrode Variance Tolerance	O	X	X	X	X	O
Energy / bit	0.24nJ/b	0.15nJ/b	0.079-0.43nJ/b	4.8nJ/b	1.4nJ/b	0.55nJ/b
Power Consumption	2.4mW	9.02mW	6.3mW	8.4mW	1.4mW	1.1mW
Area	12.5mm^2	1.12mm^2	5.93mm^2	12.5mm^2	2.13mm^2	0.542mm^2
Data Rate	10kb/s-10Mb/s	60Mb/s	100kb/s,80Mb/s	164kb/s-1.3125Mb/s	1Mb/s	200Kb/s-2Mb/s
Sensitivity	-66dBm	-58dBm	-58dBm,-72dBm	-98.3dBm	-	-83.1dBm
BER	10^{-5}@10Mb/s 10^{-12}@10kb/s	< 10^{-5}	10^{-5}	-	-	10^{-7}@2Mb/s 10^{-10}@200Kb/s

V. CONCLUSION

The proposed P-OFDM TRX for the (HBAN) alleviates the effects of environmental variables on the BCC channel quality. It also tackles the variable ground effect, variable skin-electrode contact impedance, signal multipath, and interference issues, all at once. An 8-point IFFT/FFT with no FPMs is utilized in P-OFDM TRX that reduces the gate count by 54% compared to the conventional FPMs. A glitch-free FSK DEM RX with VTL and all digital cycle correction is proposed to support a scalable data rate (200 Kbps–2 Mbps). The proposed P-OFDM TRX is implemented in 65-nm-1P7M CMOS process implemented in 65-nm CMOS with an active area of 0.54 mm^2 and consumes 1.1 mW.

REFERENCES

[1] V. Mihajlovic *et al.*, "Wearable, wireless EEG solutions in daily life applications: What are we missing?" *IEEE J. Biomed. Health Inform.*, vol. 19, no. 1, pp. 6–21, Jan. 2015.

[2] M. Swan, "Sensor mania! The Internet of Things, wearable computing, objective metrics, and the quantified self 2.0," *J. Sens. Actuator Netw.*, vol. 1, no. 3, pp. 217–253, Nov. 2012.

[3] M. A. B. Altaf, C. Zhang, and J. Yoo, "A 16-channel patient-specific seizure onset and termination detection SoC with impedance-adaptive transcranial electrical stimulator," *IEEE J. Solid-State Circuits*, vol. 50, no. 11, pp. 2728–2740, Nov. 2015.

[4] D. J. Rodriguez, A. Afzal, R. Evonich, and D. E. Haines, "The prevalence of methicillin resistant organisms among pacemaker and defibrillator implant recipients," *Amer. J. Cardiovasc. Disease*, vol. 2, no. 2, pp. 116–122, May 2012.

[5] W. Saadeh, M. Altaf, H. Alsuradi, and J. Yoo, "A pseudo OFDM with miniaturized FSK demodulation body coupled communication transceiver for binaural hearing aids in 65 nm CMOS," *IEEE J. Solid-State Circuits*, vol. 52, no. 3, pp. 757–768, Mar. 2017.

[6] M. Lont, *Wake-up Receiver Based Ultra-Low-Power WBAN*. Cham, Switzerland: Springer, 2014.

[7] (Feb. 2015). N. Hunn. *The Market for Smart Wearable Technology A Consumer Centric Approach*. [Online]. Available: http://www.nickhunn.com/wp-content/uploads/downloads/2014/08/The-Market-for-Smart-Wearables.pdf

[8] T. Zasowski, G. Meyer, F. Althaus, and A. Wittneben, "UWB signal propagation at the human head," *IEEE Trans. Microw. Theory Techn.*, vol. 54, no. 4, pp. 1836–1845, Jun. 2006.

[9] N. Cho, J. Yoo, S.-J. Song, J. Lee, S. Jeon, and H.-J. Yoo, "The human body characteristics as a signal transmission medium for intrabody communication," *IEEE Trans. Microw. Theory Techn.*, vol. 55, no. 5, pp. 1080–1086, May 2007.

[10] T. G. Zimmerman, "Personal area networks: Near-field intrabody communication," *IBM Syst. J.*, vol. 35, no. 3, pp. 609–617, 1996.

[11] R. Chandra and A. J. Johansson, "A link loss model for the on-body propagation channel for binaural hearing aids," *IEEE Trans. Antennas Propag.*, vol. 61, no. 12, pp. 6180–6190, Dec. 2013.

[12] J. Bae, K. Song, H. Lee, H. Cho, and H.-J. Yoo, "A 0.24-nJ/b wireless body-area-network transceiver with scalable double-FSK modulation," *IEEE J. Solid-State Circuits*, vol. 47, no. 1, pp. 310–322, Jan. 2012.

[13] H. Cho, H. Lee, J. Bae, and H.-J. Yoo, "A 5.2 mW IEEE 802.15.6 HBC standard compatible transceiver with power efficient delay-locked-loop based BPSK demodulator," *IEEE J. Solid-State Circuits*, vol. 50, no. 11, pp. 2549–2559, Nov. 2015.

[14] H. Cho *et al.*, "A 79 pJ/b 80 Mb/s full-duplex transceiver and a 42.5 µW 100 kb/s super-regenerative transceiver for body channel communication," in *IEEE Int. Solid-State Circuits Conf. (ISSCC) Dig. Tech. Papers*, Feb. 2015, pp. 380–381.

[15] J. Lee *et al.*, "A 60 Mb/s wideband BCC transceiver with 150 pJ/b RX and 31 pJ/b TX for emerging wearable applications," in *IEEE Int. Solid-State Circuits Conf. (ISSCC) Dig. Tech. Papers*, Feb. 2014, pp. 498–499.

[16] W. Saadeh, Y. Kifle, and J. Yoo, "A hybrid OFDM body coupled communication transceiver for binaural hearing aids in 65 nm CMOS," in *Proc. IEEE Int. Symp. Circuits Syst. (ISCAS)*, May 2015, pp. 2620–2623.

[17] P.-Y. Tsai, S.-Y. Hsu, J.-S. Chang, T.-W. Chen, and C.-Y. Lee, "A QPSK/16-QAM OFDM-based 29.1 Mbps LINC transmitter for body channel communication," in *Proc. IEEE Asian Solid-State Circuits Conf. (A-SSCC)*, Nov. 2012, pp. 345–348.

[18] W. Saadeh, H. Alsuradi, M. Altaf, and J. Yoo, "A 1.1 mW hybrid OFDM ground effect-resilient body coupled communication transceiver for head and body area network," in *Proc. IEEE Asian Solid-State Circuits Conf. (A-SSCC)*, Nov. 2016, pp. 201–204.

[19] J. Park and P. P. Mercier, "Magnetic human body communication," in *Proc. IEEE Eng. Med. Biol. Conf. (EMBC)*, Aug. 2015, pp. 1841–1844.

[20] M. D. Pereira, G. A. Alvarez-Botero, and F. R. de Sousa, "Characterization and modeling of the capacitive HBC channel," *IEEE Trans. Instrum. Meas.*, vol. 64, no. 10, pp. 2626–2635, Oct. 2015.

[21] M. S. Wegmueller, M. Oberle, N. Felber, N. Kuster, and W. Fichtner, "Signal transmission by galvanic coupling through the human body," *IEEE Trans. Instrum. Meas.*, vol. 59, no. 4, pp. 963–969, Apr. 2010.

[22] M. A. Callejon, D. Naranjo-Hernandez, J. Reina-Tosina, and L. M. Roa, "Distributed circuit modeling of galvanic and capacitive coupling for intrabody communication," *IEEE Trans. Biomed. Eng.*, vol. 59, no. 11, pp. 3263–3269, Nov. 2012.

[23] Ž. Lučev, I. Krois, and M. Cifrek, "A capacitive intrabody communication channel from 100 kHz to 100 MHz," *IEEE Trans. Instrum. Meas.*, vol. 61, no. 12, pp. 3280–3289, Dec. 2012.

[24] J. Park, H. Garudadri, and P. P. Mercier, "Channel modeling of miniaturized battery-powered capacitive human body communication systems," *IEEE Trans. Biomed. Eng.*, vol. 64, no. 2, pp. 452–462, Feb. 2017.

[25] Y. Kifle, H.-S. Kim, and J. Yoo, "Human body and head characteristics as a communication medium for Body Area Network," in *Proc. IEEE Eng. Med. Biol. Conf. (EMBC)*, Aug. 2015, pp. 1845–1848.

[26] J. Mao, B. Zhao, Y. Lian, and H. Yang, "The effects of GND electrodes in capacitive-coupling body channel communication," in *Proc. IEEE Biomed. Circuits Syst. (BioCAS)*, Oct. 2015, pp. 5–8.

[27] H. J. Yoo, and C. Van Hoof, *Bio-Medical CMOS ICs*, 1st ed. New York, NY, USA: Springer, 2011, pp. 350–353.

[28] J. Yoo and H.-J. Yoo, "Fabric circuit board-based dry electrode and its characteristics for long-term physiological signal recording," in *Proc. IEEE Eng. Med. Biol. Conf. (EMBC)*, Sep. 2011, pp. 2497–2500.

[29] M. Altaf and J. Yoo, "A 2.45 µW patient-specific non-invasive transcranial electrical stimulator with an adaptive skin-electrode impedance monitor," in *Proc. IEEE Biomed. Circuits Syst. (BioCAS)*, Oct. 2015, pp. 270–273.

[30] N. Cho *et al.*, "A 60 kb/s-to-10 Mb/s 0.37 nJ/b adaptive-frequency-hopping transceiver for body-area network," *IEEE J. Solid-State Circuits*, vol. 44, no. 3, pp. 708–717, Mar. 2009.

[31] R.-M. Weng, S.-Y. Li, and J.-C. Wang, "Low power frequency-shift keying demodulators for biomedical implants," in *Proc. IEEE Electron Devices Solid-State Circuits (EDSSC)*, Dec. 2007, pp. 1079–1082.

[32] S. Song *et al.*, "A 4.9 mΩ-sensitivity mobile electrical impedance tomography IC for early breast-cancer detection system," *IEEE J. Solid-State Circuits*, vol. 50, no. 1, pp. 245–257, Jan. 2015.

[33] S. Kim *et al.*, "A 20 µW intra-cardiac signal-processing IC with 82 dB bio-impedance measurement dynamic range and analog feature extraction for ventricular fibrillation detection," in *IEEE Int. Solid-State Circuits Conf. (ISSCC) Dig. Tech. Papers*, Feb. 2013, pp. 302–303.

Wala Saadeh (S'12–M'16) received the B.S. degree from the Computer Engineering Department, Yarmouk University, Irbid, Jordan, in 2009, and the M.Sc. degree in microsystems engineering and Ph.D. degree in interdisciplinary program from the Masdar Institute of Science and Technology, Abu Dhabi, United Arab Emirates, in 2012 and 2016, respectively.

In 2013, she joined Test-Chip Integration team, Global Foundries, Dresden, Germany, as a Test-Chip intern, where she performed quality assurance tests on advanced nodes for DFM. She developed a low-energy body-area-network transceiver for binaural hearing aid for long-term continuous monitoring. Since 2016, she has been with the Electrical Engineering Department, Lahore University of Management Sciences, Lahore, Pakistan, where she is currently an Assistant Professor. Her current research interests include ultra-low power wearable devices, human gait analysis for elderly people, and system-on-a-chip design for portable medical devices.

Dr. Saadeh was a recipient of the IEEE International Symposium on Circuits and Systems (ISCAS) 2015 Best Paper Award (BioCAS Track) and the ISCAS 2015 Runner-Up Best Student Paper Award.

Muhammad Awais Bin Altaf (S'11–M'16) received the B.S. degree from the University of Engineering and Technology, Lahore, Pakistan, in 2008, and the M.Sc. and Ph.D. degrees in microsystems engineering and interdisciplinary engineering from the Masdar Institute of Science and Technology (MIST), Abu Dhabi, United Arab Emirates, in 2012 and 2016, respectively.

From 2012 to 2013, he was a Digital Design Engineer Intern at Design Solutions, Global Foundries, Dresden, Germany, where he was involved in the implementation of digital test chips in support of 20 and 14 nm technologies. In 2015, he joined the Massachusetts Institute of Technology, Cambridge, MA, USA, as an Exchange-Ph.D. Student, where he developed an energy efficient machine-learning-based feature extraction and classification processor for epileptic seizure detection. Since 2016, he has been with the Electrical Engineering Department, Lahore University of Management Sciences, Lahore, where he is currently an Assistant Professor. His current research interests include physiological signal monitoring, breast cancer detection, and the development of low-power mixed-signal circuits for the portable medical applications.

Haneen Alsuradi (S'13) received the B.Sc. degree in electrical and electronics engineering with a minor in applied physics from the University of Sharjah, Sharjah, United Arab Emirates, in 2014, and the M.Sc. degree in electrical engineering and computer science (EECS) from the Masdar Institute of Science and Technology (MIST), Abu Dhabi, United Arab Emirates, in 2016.

She is currently a Research Engineer with the Microsystems Program, Department of EECS, MIST. Her current research interests include the modeling and fabrication of passive components on flexible substrate, including medical hydrocolloids.

Jerald Yoo (S'05–M'10–SM'15) received the B.S., M.S., and Ph.D. degrees from the Korea Advanced Institute of Science and Technology, Daejeon, South Korea, in 2002, 2007, and 2010, respectively.

From 2010 to 2016, he was with the Department of Electrical Engineering and Computer Science, Masdar Institute, Abu Dhabi, United Arab Emirates, where he was an Associate Professor. From 2010 to 2011, he was also with the Microsystems Technology Laboratories, Massachusetts Institute of Technology as a visiting scholar. Since 2017, he has been with the Department of Electrical and Computer Engineering, National University of Singapore, Singapore, where he is currently an Associate Professor. He has developed low-energy body-area-network (BAN) transceivers (TRX) and wearable body sensor network using planar-fashionable circuit board for continuous health monitoring system. He has authored a book chapter in *Biomedical CMOS ICs* (Springer, 2010) and *Enabling the Internet of Things— From Circuits to Networks* (Springer, 2017). His current research interests include low-energy circuit technology for wearable bio signal sensors, flexible electronics, BAN TRXs, ASIC for piezoelectric micromachined ultrasonic transducers, and system-on-a-chip design to system realization for wearable healthcare applications.

Dr. Yoo was a recipient or a co-recipient of several awards: the IEEE International Circuits and Systems (ISCAS) 2015 Best Paper Award (BioCAS Track), the ISCAS 2015 Runner-Up Best Student Paper Award, the Masdar Institute Best Research Award in 2015, and the Asian Solid-State Circuits Conference (A-SSCC) Outstanding Design Awards in 2005. He was the Vice Chair of the IEEE Solid-State Circuits Society United Arab Emirates Chapter. He serves as a Technical Program Committee Member of the IEEE A-SSCC, the IEEE Custom Integrated Circuits Conference, and the IEEE International Solid-State Circuits Conference Student Research Preview. He is also an Analog Signal Processing Technical Committee Member of the IEEE Circuits and Systems Society. He is a Distinguished Lecturer of the IEEE Solid-State Circuits Society.